**Journal of Korean Powder Metallurgy Institute**
Vol. 9, No. 6, 2002

# High Strength Nanostructured Metastable Alloys

**Jürgen Eckert, Birgit Bartusch, Frank Schurack, Guo He and Ludwig Schultz**
*IFW Dresden, Institut für Metallische Werkstoffe, Postfach 27 00 16, D-01171 Dresden, Germany*
(Received 30 October 2002 ; Accepted form 5 December 2002)

**Abstract** Nanostructufed high strength metastable Al-, Mg- and Ti-based alloys containing different amorphous, quasicrystalline and nanocrystalline phases are synthesized by non-equilibrium processing techniques. Such alloys can be prepared by quenching from the melt or by powder metallurgy techniques. This paper focuses on one hand on mechanically alloyed and ball milled powders containing different volume fractions of amorphous or nano-(quasi)crystalline phases, consolidated bulk specimens and, on the other hand, on cast specimens containing different constituent phases with different length-scale. As one example, $Mg_{55}Y_{15}Cu_{30}$-based metallic glass matrix composites are produced by mechanical alloying of elemental powder mixtures containing up to 30 vol.% $Y_2O_3$ particles. The comparison with the particle-free metallic glass reveals that the nanosized second phase oxide particles do not significantly affect the glass-forming ability upon mechanical alloying despite some limited particle dissolution. A supercooled liquid region with an extension of about 50 K can be maintained in the presence of the oxides. The distinct viscosity decrease in the supercooled liquid regime allows to consolidate the powders into bulk samples by uniaxial hot pressing. The $Y_2O_3$ additions increase the mechanical strength of the composites compared to the $Mg_{55}Y_{15}Cu_{30}$ metallic glass. The second example deals with Al-Mn-Ce and Al-Cu-Fe composites with quasicrystalline particles as reinforcements, which are prepared by quenching from the melt and by powder metallurgy. $Al_{98-x}Mn_xCe_2$ (x = 5, 6, 7) melt-spun ribbons containing a major quasicrystalline phase coexisting with an Al-matrix on a nanometer scale are pulverized by ball milling. The powders are consolidated by hot extrusion. Grain growth during consolidation causes the formation of a micrometer-scale microstructure. Mechanical alloying of $Al_{63}Cu_{25}Fe_{12}$ leads to single-phase quasicrystalline powders, which are blended with different volume fractions of pure Al-powder and hot extruded forming $Al_{100-x}(Al_{0.63}Cu_{0.25}Fe_{0.12})_x$ (x = 40, 50, 60, 80) micrometer-scale composites. Compression test data reveal a high yield strength of $\sigma_y \geq 700$ MPa and a ductility of $\varepsilon_{pl} \geq 5\%$ for than the Al-Mn-Ce bulk samples. The strength level of the Al-Cu-Fe alloys is $\sigma_y \leq 550$ MPa significantly lower. By the addition of different amounts of aluminum, the mechanical properties can be tuned to a wide range. Finally, a bulk metallic glass-forming Ti-Cu-Ni-Sn alloy with *in situ* formed composite microstructure prepared by both centrifugal and injection casting presents more than 6% plastic strain under compressive stress at room temperature. The *in situ* formed composite contains dendritic *hcp* Ti solid solution precipitates and a few $Ti_3Sn$, β-(Cu, Sn) grains dispersed in a glassy matrix. The composite microstructure can avoid the development of the highly localized shear bands typical for the room temperature deformation of monolithic glasses. Instead, widely developed shear bands with evident protuberance are observed, resulting in significant yielding and homogeneous plastic deformation over the entire sample.

**Keywords:** nanostructured metastable materials, metallic glasses, quasicrystals, composites, mechanical alloying, liquid quenching, thermal stability, viscosity, powder consolidation, mechanical properties.

## 1. Introduction

Scientific curiosity has continuously driven materials scientists towards improving the properties and performance of structural and functional materials. Moreover, for example the need for high strength and low density materials for the aerospace and automotive industry has raised a lot of research activities devoted to the development of high strength lightweight materials during the past thirty years[1]. Besides the

improvements achieved through modification of alloy chemistry and conventional processing methods, the ever increasing demand for improved materials has led to the design and development of advanced materials. It is now well recognized that the structure and the constitution of advanced materials can be precisely tailored by processing them under non-equilibrium conditions[2]. Among processes like rapid solidification from the melt, plasma processing or vapor deposition, mechanical alloying of elemental powder mixtures (MA) and ball milling (BM) of pre-alloys have received increasing attention from the scientific as well as from the industrial community. The general underlying idea for all these techniques is to synthesize materials in a non-equilibrium state by "energizing and/or quenching"[3]. In case of MA and BM the energization is achieved through solid state powder processing involving repeated cold welding, fracturing and re-welding of powder particles in a high energy ball mill. Originally developed to produce oxide dispersion strengthened (ODS) nickel- and iron-base superalloys by Benjamin *et al.*[4], MA/BM has been shown to be a versatile tool for synthesizing a variety of equilibrium and non-equilibrium phases including e.g. supersaturated solid solutions, nanocrystalline phases, quasicrystalline materials and amorphous alloys[3].

One of the most promising class of alloys for application as novel advanced materials with quite unique combination of properties are bulk glass-forming metallic alloys (mostly called bulk metallic glasses (BMGs) or bulk amorphous alloys (BAA)), which have been progressively developed in the past decade (for recent overview on the development of BMGs see[5,6]. BMGs usually exhibit very good mechanical properties, such as high hardness and yield strength, large elastic strain limit and a high wear resistance[5,6]. Due to their high glass-forming ability and high thermal stability of the supercooled liquid against crystallization, they allow for the production of bulk samples by casting[7,8] or by mechanical alloying followed by powder compaction in the viscous state above the glass transition temperature[9,10]. However, BMGs exhibit inhomogeneous deformation behavior for temperatures below the glass transition temperature[11]. All the plastic flow is concentrated in one or several shear bands. Further deformation leads to a softening in the localized bands, with the result that the final fracture occurs along the planes of those softened shear bands. This inhomogeneous deformation, unfortunately, leads to catastrophic failure with little plastic elongation in an apparently brittle manner. To prevent inhomogeneous deformation, i.e. to hinder shear band propagation and to impede deformation[12-14], three methods have been introduced so far, which are particle reinforcement[15-17], fiber reinforcement[13,18-20] and *in situ* formed ductile phase precipitates[21-23]. The latter method can significantly enhance the room temperature ductility of BMGs by introducing a ductile phase, which usually has a β-Ti-type cubic structure and dendritic morphology. So far, most of the efforts for reinforcements were focused on Zr-base BMGs because these alloys have a high glass-forming ability. The elastic strain is about 2-3% for single-phase Zr-base BMGs at room temperature, and the macroscopic plastic strain is almost zero prior to failure[24]. After introducing the ductile dendritic β-Ti-type phase, the plastic strain can reach 6-7% in compression and about 3% in tension for Zr-Nb-Ti-Cu-Ni-Be[21,22]. Recently, 16% compression plastic strain were obtained in a Zr-Ni-Cu-Al-Ta alloy[25].

However, second phase particles can trigger heterogeneous nucleation upon quenching from the melt, thus deteriorating the castability and the thermal stability of the metallic glass[13]. Moreover, restrictions may arise in the preparation of cast bulk samples with constituents having large difference of melting point or density, such as metals and oxides. In contrast, mechanical alloying as a special form of solid state reaction technique circumvents these restrictions and allows to obtain composites in which ceramic particles are embedded in a glassy matrix[16,26-28].

Another class of materials with very interesting properties for use as advanced materials are quasicrystal-forming alloys. From a large number of investigations[29-32] quasicrystalline materials are known to exhibit high hardness and high strength, exceeding the strength of conventional precipitation and solid solution hardened Al-alloys by a factor of 2-4[33]. Up to the brittle-to-ductile transition at around 0.8 of the melting temperature the mechanical behavior of quasicrystals appears to be ceramic-like[33]. The high room temperature brittleness of quasicrystals is the main reason for the limitation of their practical importance as engineering materials so far.

In order to exploit the mechanical properties, quasicrystals have been used as reinforcements in metal-matrix composites. According to the strengthening mechanism, different types of composites can be distinguished. For example, nanosized quasicrystals

finely dispersed in a solid solution matrix were found to act as pinning centers for dislocations in an AlLi-CuMg alloy[34] and in a maraging steel[35]. In 1992, tensile strengths of more than 1 GPa were reported for melt-spun Al-Mn-Ce and Al-Mn-Fe[36,37] alloys. The microstructure of these alloys is characterized by quasicrystalline precipitates of about 50-100 nm in size, which are surrounded by a thin film of Al-matrix. Later attempts to reproduce a similar microstructure in bulk samples *in situ* by powder metallurgical methods, such as gas atomization and mechanical alloying[38,39], led to micrometer-scale composites instead.

Another concept, which is similar to the one of metal-matrix composites with ceramic particles, utilizes quasicrystalline particles with a size of more than 10 μm in order to deflect the stress from the ductile matrix and to minimize the overall deformable volume fraction. In contrast to the described nanoscale composites, which form *in situ*, the components are separately prepared and mixed in a subsequent step. Such composites were prepared via powder metallurgy in the Al-Cu-Fe system by Tsai *et al.*[40] resulting in an increase of the hardness of pure aluminum by a factor of 3. Recently, such materials were also synthesized by casting an aluminum melt containing gas atomized quasicrystalline Al-Cu-Fe powders[41,42]. The focus on Al-Cu-Fe alloys is mainly due to the fact that there is a stable quasicrystalline phase in this alloy system[43].

The present paper reviews some of our recent efforts in applying non-equilibrium techniques to synthesize nanostructured metastable alloys providing a tailored set of mechanical properties to meet high strength lightweight applications. The approach is exemplified by three different case studies:

(1) Mechanically alloyed $Mg_{55}Y_{15}Cu_{30}$-based metallic glass matrix composites with up to 30 vol.% nanosized $Y_2O_3$ particles as a representative for novel Mg-based lightweight BMG alloys containing nanoscale oxide phases. We will report on the phase formation and the properties of these composites and compare the data for the composites with the dispersoid-free glass.

(2) Quasicrystal-reinforced aluminum alloys as examples for materials containing quasicrystals, where we will review the microstructure and the mechanical properties of two types of quasicrystal-reinforced aluminum-matrix composites. Al-Mn-Ce composites are created by pulverization of melt-spun ribbons via ball milling and consolidation of the powders by hot extrusion. Furthermore, single-phase quasicrystalline powders are synthesized by mechanical alloying and blended with pure aluminum powder. The mechanical properties obtained from room temperature compression tests will be discussed with respect to the differences in the microstructure and compared with those of cast bulk specimens[44].

(3) Finally, we will report on Ti-base bulk metallic glass-forming alloys with *in situ* formed composite microstructure as a potential candidate for *in situ* formed BMG composites containing ductile precipitates. The composite microstructure includes mainly a dendritic *hcp* Ti solid solution, a small amount of intermetallic $Ti_3Sn$ as well as β-(Cu, Sn) dispersed in the glassy matrix. This composite microstructure can avoid the development of highly localized shear bands under load. Accordingly, deformation occurs via the development of normally ductile patterns of regularly spaced shear bands distributed homogeneously throughout the whole sample, which allows for nearly 6% compressive plastic strain before failure at room temperature.

These types of materials were selected because they show a huge potential for application as new and advanced high-strength lightweight materials for a variety of technology fields. Particular attention will be paid to not only to the formation of phases and microstructures with tailored properties, but also to the influence of the processing conditions on phase formation and the interplay between microstructure and mechanical properties.

## 2. Experimental Procedure

For obtaining Mg-Y-Cu-based BMG composites with up to 30 vol.% of oxides, Mg, Y and Cu powders (purity 99.9%, particle size $< 150$ μm) were mixed to give a composition of $Mg_{55}Y_{15}Cu_{30}$ and blended with $Y_2O_3$ particles (purity 99.9%, particle size 1.52.5 μm). For the quasicrystal-reinforced samples, Al-Mn-Ce prealloys were prepared by arc-melting pure metals with nominal purities of $> 99.9$ at.%. Melt spinning was performed using a modified Bühler melt-spinner. Ribbons with a cross section of $10 \times 0.02$ mm$^2$ were produced. The mechanical alloying started from elemental Al, Cu and Fe powders with nominal purities of $> 99.9$ at.% (particle size $< 150$ μm). All powder handling was done in a glove box under argon atmosphere ($O_2$, $H_2O < 1$ ppm). The powders were milled in a RETSCH planetary ball mill using hardened steel

milling tools at a rotational speed of 180 rpm and a ball-to-powder weight ratio of 13 : 1. Inductively-coupled plasma optical emission spectroscopy (ICP-OES) and atomic-absorption spectroscopy (AAS) of the as-milled powders revealed deviations of about ± 0.3 at.% from the nominal compositions and iron impurity of less than 0.5 at.% due to wear debris from the milling tools. Non-metallic impurities like oxygen and nitrogen, which mainly stem from the starting materials, were determined by hot extraction (C436 LECO analyzer) to be about 0.4 and 0.2 at.%, respectively. For the Ti-base bulk metallic glass-forming alloys with *in situ* formed composite microstructure, we selected $Ti_{50}Cu_{23}Ni_{20}Sn_7$ which has the largest glass-forming ability reported for Ti-base BMGs so far,[45,46] for investigation. Since it is well known that the microstructure of alloys depends on the applied casting conditions, we used different methods to prepare the master alloy and for casting the cylinders. The master alloys were obtained by arc melting of a mixture of the pure metals. The cast cylinders with 50 mm length and 2 or 3 mm in diameter were prepared by injection casting and centrifugal casting, respectively. For comparison, 40 μm thick ribbons were prepared by melt spinning.

Structural characterization was done by X-ray diffraction (XRD)(Philips PW 1050 diffractometer; Co-Kα radiation or Philips PW 1040 diffractometer Cu-Kα radiation), transmission electron microscopy (TEM) employing JEOL 2000FX and Philips CM20 FEG analytical microscopes both with 200 kV acceleration voltage, and scanning electron microscopy (SEM) using a a Jeol JSM 6400 microscope, respectively. The thermal stability and the crystallization behavior of the different samples was investigated by constant-rate heating at 20 or 40 K/min and isothermal annealing in a flow of purified argon using a Perkin-Elmer DSC7 calorimeter. The viscosity of the powders was analyzed by parallel plate rheometry in a Perkin-Elmer thermal-mechanical analyzer (TMA7) with quartz penetration probe at a static load of 2.6 N under argon atmosphere at a heating rate of 10 K/min. Before the measurements, the samples were annealed above the glass transition temperature $T_g$ to obtain relaxed isoconfigurational states. The powders were either consolidated in a uniaxial hot press under vacuum at pressures of 400-500 MPa or by extrusion at 623 K under a vacuum of about $2 \times 10^{-5}$ mbar with an extrusion ratio of 6 : 1 using the same hot press facility with an extrusion accessory. Before, the powders were manually cold pressed to green bodies and encapsulated into copper cans. The Vickers microhardness $H_v$ was measured at room temperature with a Neophot hardness tester and a load of 0.2 N was applied for 10 s. The mechanical properties were tested by compression tests. Cylindrical specimens of 4 mm in diameter and a height of 8 mm were prepared from the bulks and deformed under a constant compression rate of $\varepsilon = 10^{-4}\ s^{-1}$ using an Instron 8562 dynamic testing system.

## 3. Results and Discussion

### 3.1. Mg-Y-Cu-Based Metallic Glass Composites

3.1.1. Microstructure Formation

Figure 1 shows typical XRD patterns of MA $Mg_{55}Y_{15}Cu_{30}$ powders blended with up to 30 vol.% of $Y_2O_3$. The patterns display the diffraction peaks of $Y_2O_3$ superimposed on the broad scattering maxima of the amorphous phase even after a long milling time. Besides, some traces of unreacted Mg, Y and Cu are visible, together with some $Y_2O_3$ peaks even in the oxide-free powder, which is due to the high reactivity of the powders[28]. The intensity of the $Y_2O_3$ peaks increases with increasing volume fraction of particles, indicating that the oxides do not significantly dissolve in the glassy matrix. However, the presence of oxide particles reduces the milling time required for complete amorphization to the half, i.e. to 50 h compared to 100 h

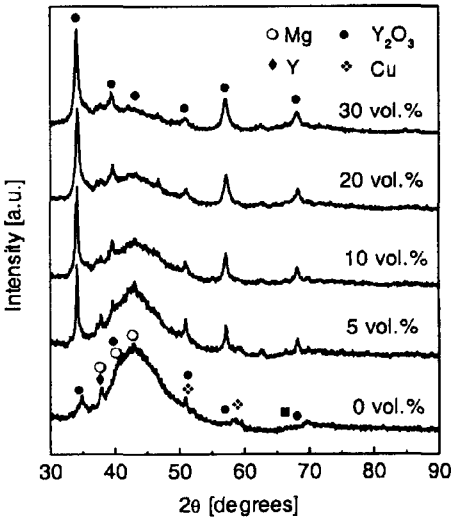


**Fig. 1. XRD patterns (Co-Kα) for $Mg_{55}Y_{15}Cu_{30}$ MA powders with different volume fractions of $Y_2O_3$ particles after 50 h of milling.**

for the dispersoid-free material. No measurable shift of the amorphous maxima is observed after long milling, suggesting again that no strong dissolution of the $Y_2O_3$ particles and, hence, no significant shift of the matrix composition occurs.

TEM investigations confirmed a homogeneous distribution of the $Y_2O_3$ particles with an approximate size of 5-10 nm in the glassy matrix. This is exemplified in Fig. 2 for $Mg_{55}Y_{15}Cu_{30}$ powder containing 5 vol.% $Y_2O_3$. The diffraction pattern shows the diffraction spots of the $Y_2O_3$ dispersoids besides the typical diffuse halo of the amorphous phase. Similar results were found for different oxide particles in the same $Mg_{55}Y_{15}Cu_{30}$ matrix[47] and also for Zr-based metallic glass matrix composites[26].

The thermal stability of the composites was investigated by DSC. All the DSC scans for 50 h milled and relaxed $Mg_{55}Y_{15}Cu_{30}$ powders mixed with up to 30 vol.% $Y_2O_3$ particles and for the particle-free metallic glass after 100 h of mechanical alloying exhibit an endothermic event due to the glass transition followed by two exothermic crystallization peaks. The primary crystallization leads to precipitation of $Mg_2Cu$ nanocrystals[28,47]. The glass transition temperatures $T_g$ and the crystallization temperatures $T_x$ (defined as the onset temperatures of the respective endothermic and exothermic heat flow events) for the samples with different volume fractions of oxide particles found for constant-rate heating at 40 K/min are in the range of 439 to 443 K and 493 to 497 K, respectively (Fig. 3). Whereas $T_g$ remains almost constant even for large volume fractions of dispersoids, the data suggest that there may be a slight increase in $T_x$ with increasing oxide volume fraction. This points to some particle dissolution in the metallic glass upon milling, similar as it has been observed for MA Zr-based metallic glass matrix composites[48]. Even limited particle dissolution will change the composition of the glassy matrix and, in turn, explains the slight increase in thermal stability of the composite samples, especially for high volume fractions of particles. However, there is no significant change in the extension of the supercooled liquid region $\Delta T_x = T_x - T_g$.

Isothermal annealing at temperatures $T = T_x - 40$ K has been performed to study the influence of the oxide particles on the thermal stability of the composites in more detail. The composites transform faster than the particle-free glass, as expressed by a shorter incubation time for crystallization and by a steeper increase of the crystallized volume fraction $x(t)$ for 5 and 30 vol.% $Y_2O_3$ (Fig. 4). Furthermore, the crystallization rate $dx/dt$ increases with increasing volume fraction. The maximum of the transformation rate occurs at shorter times, i.e. for a $Y_2O_3$ volume fraction of $v_f = 0$ at 60 min, for $v_f = 5$ at 34 min and for $v_f = 30$ at 28 min. The details of the isothermal DSC investigations are still not fully understood and will be a topic for future investigations. Nevertheless, the thermal stability of the composite samples is sufficient for compaction into bulk specimens without crystallization of the glassy matrix.

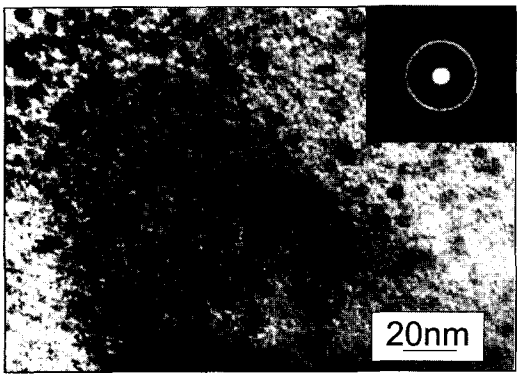


**Fig. 2. TEM bright-field image and corresponding diffraction pattern of a $Mg_{55}Y_{15}Cu_{30}$ 5 vol.% $Y_2O_3$ MA powder after 50 h of milling.**

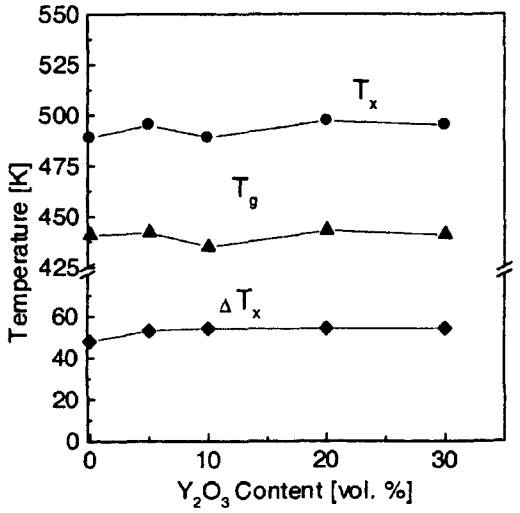


**Fig. 3. Thermal stability data of $Mg_{55}Y_{15}Cu_{30}$ and the composite powders as a function of the $Y_2O_3$ volume fraction (heating rate 40 K/min).**

3.1.2. Viscosity Measurements and Powder Consolidation

Figure 5 shows the relative viscosity $\eta_{rel} = \eta/\eta_{0,min}$, where $\eta_{0,min}$ is the minimum value of viscosity measured for the particle-free glass, for $Mg_{55}Y_{15}Cu_{30}$ composite powders with different volume fractions of $Y_2O_3$ particles as a function of temperature in comparison with the viscosity for the dispersoid-free $Mg_{55}Y_{15}Cu_{30}$ glass. The measured viscosity $\eta$ is an effective viscosity due to the contribution of the nano-sized $Y_2O_3$ particles in the supercooled liquid and the fractions of unreacted material[49]. For all samples, the viscosity first decreases with increasing temperature upon heating from the amorphous solid through the glass transition into the supercooled liquid state. At higher temperatures the viscosity increases again due to crystallization. The minimum viscosities are on the order of magnitude of $10^8$ Pa*s and are consistent with the data for cast MgYCu BMGs[50] and for other glass matrix composites[12,16,26]. Volume fractions of more than 5 vol.% $Y_2O_3$ lead to a slight viscosity increase and to differences in the thermal behavior, which are related to partial dissolution of oxides and a retardation of viscous flow. The differences in the minimum viscosity and the flow behavior between the dispersoid-free glass and the composites are rather small, indicating that the effective viscosity of the material is not drastically affected by the presence of up to 30 vol.% $Y_2O_3$ dispersoids.

The existence of an extended supercooled liquid region together with the decrease of the viscosity above $T_g$ enables the consolidation of the milled powders into bulk samples of 10 mm in diameter and 6 mm in height by uniaxial hot pressing. The consolidation was performed at a temperature of $T_x$ - 40 K in order to use the decrease in viscosity above $T_g$, but also to avoid isothermal crystallization. The comparison of as-milled

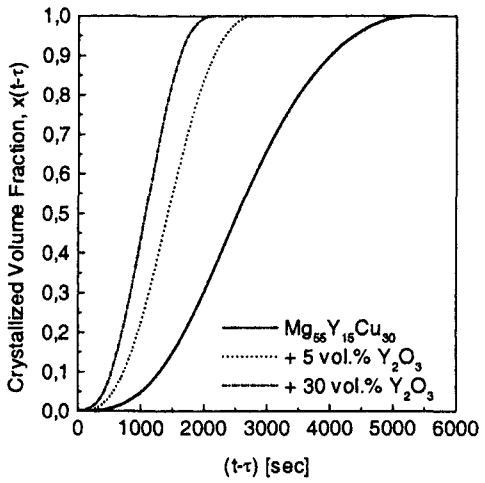


**Fig. 4. Crystallized volume fraction $x$ $(t-\tau)$ for the particle-free and $Y_2O_3$-containing samples.**

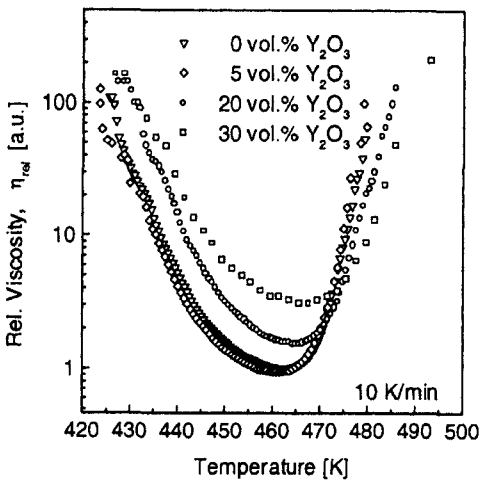


**Fig. 5. Relative viscosity for MA $Mg_{55}Y_{15}Cu_{30}$ with different volume fraction of $Y_2O_3$ particles as a function of temperature (heating rate 10 K/min).**

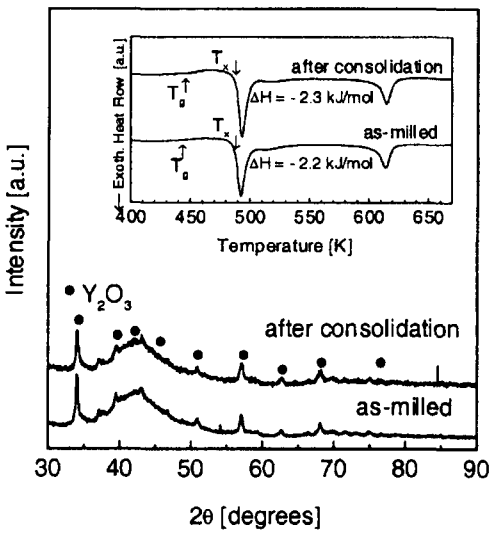


**Fig. 6. XRD patterns (Co-Kα) for as-milled $Mg_{55}Y_{15}Cu_{30}$-5 vol.% $Y_2O_3$ powder and for the consolidated bulk sample (inset: corresponding DSC scans obtained at a heating rate 40 K/min).**

powder and bulk samples by XRD analysis (Fig. 6) gave no hint for crystallization during consolidation. Furthermore, similar features and almost equal enthalpies for the primary crystallization are visible in the inset of Fig. 6 for the $Mg_{55}Y_{15}Cu_{30}$-5 vol.% $Y_2O_3$ composite as an example. These results confirm that the phase composition remains unchanged upon consolidation. Density measurements reveal that the bulk samples are more than 99.5% dense.

3.1.3. Mechanical Properties

The mechanical properties of the bulk samples were characterized by Vickers microhardness ($H_v$) measurements and by constant strain rate compression tests. The $H_v$ data for $Mg_{55}Y_{15}Cu_{30}$ and for the composites with diff-erent volume fractions of $Y_2O_3$ are summarized in Table 1. The addition of nanoscale $Y_2O_3$ particles raises the microhardness. The suppression of shear band propagation due to nanocrystalline precipitates in the amorphous matrix is probably the reason for this increase in microhardness, similarly observed for nanocrystalline metallic precipitates in a glassy Zr-based matrix[26].

The influence of the $Y_2O_3$ nanoparticles on the yield strength was investigated for bulk $Mg_{55}Y_{15}Cu_{30}$ composite samples with 0, 5 and 20 vol.% $Y_2O_3$. Figure 7 shows curves of the true stress $\sigma$ vs. the true compression $\varepsilon$ for these samples, as obtained by compression tests at a constant compression rate of $\dot{\varepsilon} = 1 \times 10^{-4}$ $s^{-1}$ at room temperature and at 423 K. All samples reach high strength values with a maximum of 709 MPa for the $Mg_{55}Y_{15}Cu_{30}$-5 vol.% $Y_2O_3$ composite. However, they exhibit no plasticity at room temperature. Possibly, the measured failure stresses at room temperature are related to insufficiently connected particles and are, therefore, lower than the true intrinsic strength of the material. Nevertheless, the room temperature strengths of these samples are 1.5-2.5 times higher than the strength of conventional Mg-based cast alloys[33]. The

**Table 1. Vickers microhardness $H_v$ for MA $Mg_{55}Y_{15}Cu_{30}$ $Y_2O_3$ composites.**

| Oxide volume fraction [vol.%] | Vickers microhardness [GPa] |
|---|---|
| 0 | 3.4 |
| 5 | 3.7 |
| 20 | 4.4 |
| 30 | 4.8 |

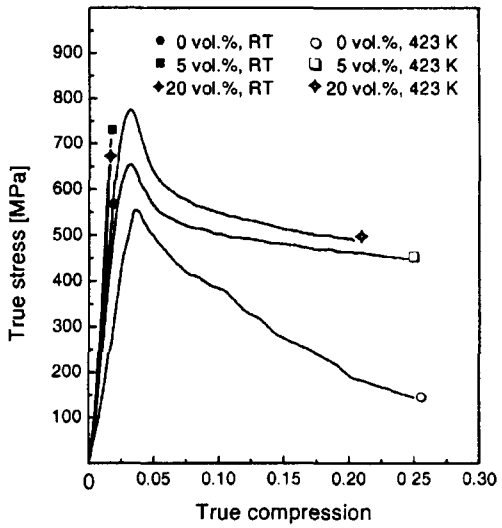


**Fig. 7. True stress vs. true compression at room temperature and at 423 K for $Mg_{55}Cu_{30}Y_{15}$ and for composites with different volume fraction of $Y_2O_3$ particles.**

possible reason for the increase in the room temperature strength of the composites is the hindering of shear band propagation by the nanocrystalline dispersoids. Young's modulus increases by the addition of the finely dispersed nanosized $Y_2O_3$ particles, e.g. from 32 GPa for the particle-free alloy to 60 GPa for the $Mg_{55}Y_{15}Cu_{30}$-5 vol.% $Y_2O_3$ composite.

The strength increase caused by the oxide particles is more pronounced at elevated temperatures (423 K) slightly below $T_g$. The curves show the typical high-temperature deformation behavior of metallic glasses[49,51]. Plastic deformation starts with a stress maximum and then declines to a steady-state flow level at plastic strains of up to 25%. The deformation behavior at temperatures near $T_g$ is mainly determined by the flow of the supercooled metallic liquid, in contrast to the room temperature deformation, which is governed by the formation and movement of localized shear bands[52].

### 3.2. Quasicrystal-reinforced Aluminum Alloys

3.2.1. Microstructure and Properties of Al-Mn-Ce Alloys

The synthesis of the metastable quasicrystalline phase in the Al-Mn-Ce system[36] requires non-equilibrium processing conditions to suppress the formation of the competing crystalline equilibrium phases $Al_{10}Mn_7Ce_2$, $Al_6Mn$ and $Al_4Ce$. The quasicrystalline

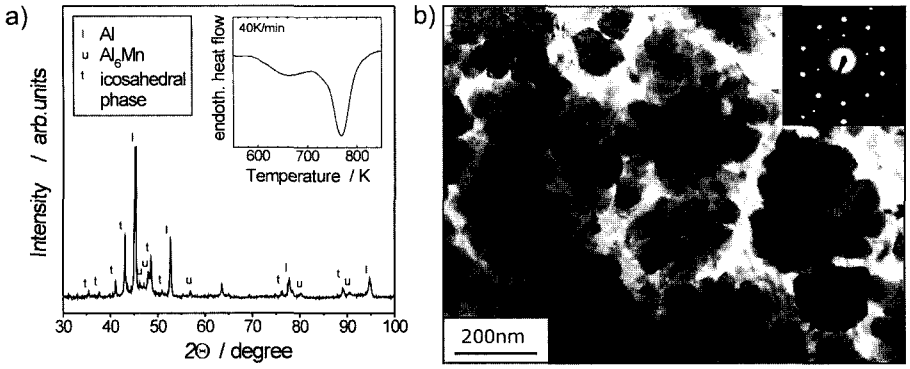


**Fig. 8 (a) XRD pattern (Co-Kα) of $Al_{92}Mn_6Ce_2$ melt-spun ribbon. Intensities are normalized to the strongest Al peak. The inset shows the corresponding DSC trace revealing the decomposition of the quasicrystalline phase. (b) Bright-field TEM image of a melt-spun $Al_{92}Mn_6Ce_2$ alloy and corresponding selected-area diffraction pattern of the precipitates along a 5-fold symmetry axis.**

phase is known to precipitate with a stoichiometry of about $Al_{88}Mn_8Ce_4$[36,44]. Therefore, the alloys were prepared starting from nominal compositions of $Al_{98-x}Mn_xCe_2$ (x = 5, 6, 7) in order to yield an Al-matrix volume fraction of around 40 vol.%.

XRD analysis, as shown exemplarily for the $Al_{92}Mn_6Ce_2$ ribbon in Fig. 8a, reveals the existence of a phase mixture of quasicrystalline phase and aluminum. Small fractions of $Al_6Mn$ equilibrium phase impurities are also visible. TEM investigations show that particles with a size of about 100-200 nm precipitated upon melt-spinning (Fig. 8b). EDX analysis proves that these particles are incorporated in an aluminum solid solution matrix. Although the morphology of the precipitates appears rather dendritic, there are also isolated particles with an average size of 50 to 100 nm. The existence of 5-fold axes as detected by electron diffraction (inset in Fig. 8b) indicates the icosahedral (i) structure of these precipitates. DSC scans show a characteristic exothermic peak (inset in Fig. 8a) with an onset temperature of $T_x$= 715 K, which was proved by XRD analysis to reflect the crystallization of the i-phase. The small exothermal heat flow signal in the temperature range from 573 to 693 K is correlated with recovery of the matrix and grain growth of both constituent phases, which was confirmed by XRD and TEM investigations on annealed samples as well as by isothermal DSC measurements. The microstructure of the other two compositions investigated differs only by the quasicrystalline volume fraction from the one of $Al_{92}Mn_6Ce_2$. In general, the results are in good agreement with previous reports of other groups[36,53].

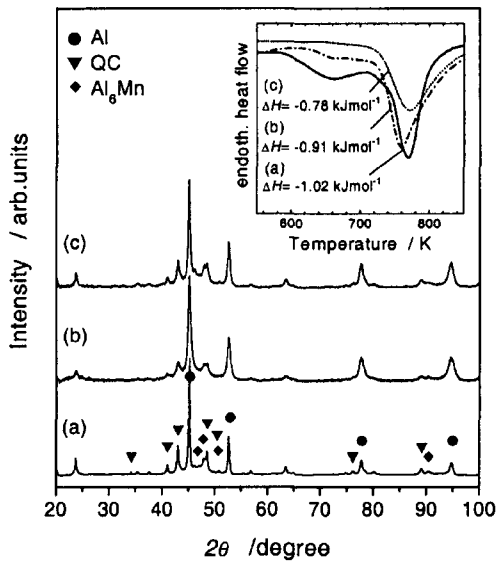


**Fig. 9. XRD patterns (Co-Kα) of $Al_{92}Mn_6Ce_2$ samples comparing the as-melt-spun state (a), the powder before (b), and after extrusion at 623 K (c). The inset shows the corresponding DSC traces with the normalized enthalpies for the transformation of the quasicrystalline phase.**

The ribbons were pulverized by crushing and subsequent BM. The application of a rather low milling intensity, i. e. milling for short times with high impact energy or vice versa, were found to be most important in order to prevent changes of the microstructure as far as possible. Therefore, the milling experiments were conducted at 300 rpm and a revolution ratio of the sun disk to the planetary disk of 1 : 2 for 30 min.

A temperature of about 623 K was chosen in order to avoid phase transformation during hot extrusion. Figure 9 shows the comparison of the XRD patterns of the as-quenched ribbon and the powder samples before and after extrusion. Besides a slight increase in the $Al_6Mn$ peak intensities there is no indication for a massive transformation of the quasicrystalline phase into the equilibrium phase(s) during consolidation. The analysis of the enthalpy release during crystallization in a DSC scan as a measure for the reacted quasicrystal volume fraction, however, implies that in fact a time-dependent reaction occurred (see inset in Fig. 9). The crystallization enthalpy decreases from 1.02 $kJmol^{-1}$ for the as-spun ribbon to 0.78 $kJmol^{-1}$ for the extruded bulk sample. This proves a partial transformation of the quasicrystals although with 623 K the temperature was kept far below the crystallization onset of 715 K, which points to a rather low activation energy for the reaction for this alloy. Hence, the total loss of quasicrystalline volume fraction during compaction was about 14 vol.%. From the disappearance of the wide exothermal signal in the DSC scan of the bulk sample before crystallization it is moreover evident that during the heat treatment upon extrusion severe grain growth can not be avoided. SEM investigations of the bulk samples revealed a microstructure as shown in Fig. 10a, which is characterized by a uniform distribution of micrometer- and submicrometer-sized precipitates in an aluminum matrix. The size distribution of the precipitates (Fig. 10b) is very homogeneous with an average particle size of about 1.4 μm.

The mechanical properties derived from true stress vs. true compression curves are given in Fig. 11. Plastic deformation starts at yield stresses of around 750 MPa. After exceeding the maximum strength moderate softening occurs, leading to a continuous decrease of the stress over almost the entire range of plastic deformation. The values for the ultimate strength range from 844 MPa for $Al_{93}Mn_5Ce_2$ to 975 MPa for $Al_{91}Mn_7Ce_2$, which is consistent with the expectation that the larger quasicrystal volume fraction in the latter alloy results in a higher strength. This goes along with the highest overall ductility of up to 23 % for the Al-rich alloy. The Young's modulus varies between 94 GPa and 102 GPa, which is significantly larger than for aluminum or for conventional aluminum alloys, yielding about 70 GPa[5]. Because of the coarser microstructure, the mechanical properties are different from those obtained from tensile tests on ribbons[8]. In Fig. 11, the stress-compression plots for $Al_{92}Mn_6Ce_2$ reference samples prepared by copper mold casting[44] and arc-melting

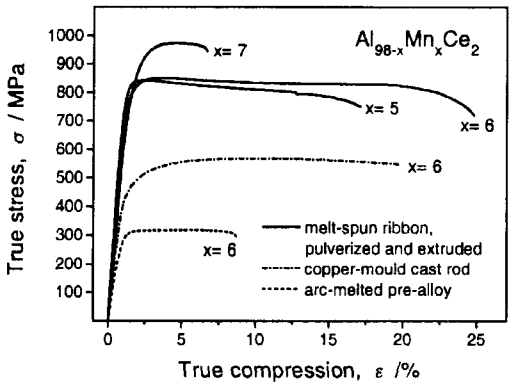


**Fig. 11. True stress vs. true compression plots obtained from room temperature constant rate compression tests of extruded powder samples with different Al-content, prepared from melt-spun ribbons. Results for the arc-melted pre-alloy and for a copper mold cast sample (taken from [44]) are given for comparison.**

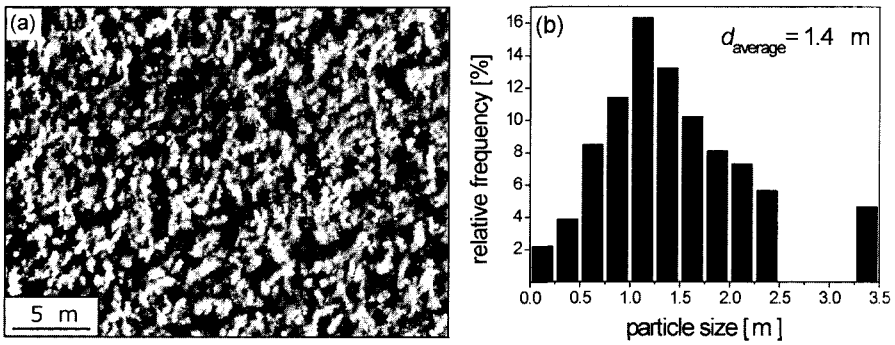


**Fig. 10. SEM image (secondary electron contrast) of the cross section of an extruded $Al_{92}Mn_6Ce_2$ alloy (a), and size distribution of the precipitates obtained from stereologic image analysis (b).**

are also shown. The remarkably lower values for the Young's modulus, the yield strength, the ultimate strength and the ductility for the cast samples illustrate primarily the influence of the particle morphology, which is much coarser and less homogeneous than in the pulverized and extruded ribbons.

3.2.2. Microstructure and Properties of Al-Cu-Fe Alloys

The preparation of a composite incorporating a stable quasicrystalline phase by MA was investigated for the AlCuFe system. Here, in contrast to most of the AlMn-based alloy systems, no two-phase region including aluminum and quasicrystalline phase exists[54,55], which prevents the *in situ* formation of a composite.

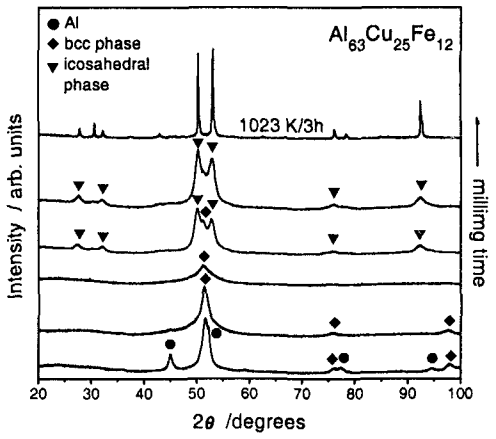


**Fig. 12. XRD patterns (Co-Kα) of mechanically alloyed $Al_{63}Cu_{25}Fe_{12}$ powders showing the evolution of a quasicrystalline phase as a function of milling time. The overall milling time was 100 h.**

Therefore, in a first step the quasicrystalline phase was synthesized by MA starting from an $Al_{63}Cu_{25}Fe_{12}$ elemental powder mixture.

The XRD patterns in Fig. 12 illustrate the phase evolution upon milling for this composition. After milling for 20 h (bottom plot) the elemental powders have been mixed and refined as indicated by the reduced intensity of the elemental peaks and the peak broadening. The appearance of interferences of a new phase with a body-centered cubic (bcc) structure (A2-type) proves that alloying of the elements has started. With increasing milling time this phase becomes the majority phase incorporating all the elements. Further milling produces an icosahedral quasicrystalline phase, which coexists initially with the bcc-phase but consumes it during the further course of milling. This results in single-phase icosahedral powder after about 100 h of milling. DSC analysis reveals that this phase is stable up to its melting point of about 1143 K. Subsequent annealing of the powder at 1023 K for 3 h results in a distinct improvement of the quasilattice perfection and grain growth. This becomes obvious from the sharpening and the intensity increase of the peaks in the XRD pattern (upper plot in Fig. 12). The detection of additional interferences proves that a face-centered superstructure of the icosahedral phase develops as it is expected for this composition[56]. This is in agreement with results of Salimon *et al.*[57] and Asahi *et al.*[58] observing the same ordering phenomenon for MA $Al_{67}Cu_{22}Fe_{11}$ and $Al_{65}Cu_{20}Fe_{15}$ powders, respectively.

The annealed $Al_{63}Cu_{25}Fe_{12}$ powders were sieved with a mesh size of 78 μm and blended with pure aluminum powder corresponding to quasicrystalline

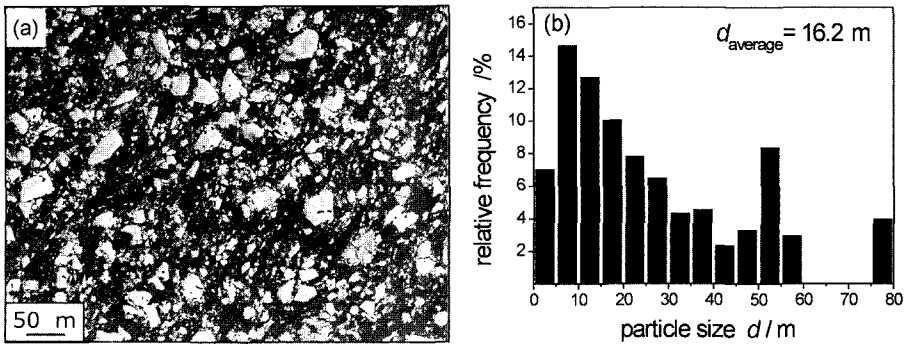


**Fig. 13. SEM image (secondary electron contrast) of the cross section of an extruded $Al_{60}(Al_{0.63}Cu_{0.25}Fe_{0.12})_{40}$ bulk sample (a). The particle size distribution (b) was obtained by stereologic image analysis.**

volume fractions of the composite of 40, 50, 60 and 80 vol.%. In order to achieve a complete coating of the particles with aluminum and for a homogeneous distribution of the particles in the matrix, the powder agglomerate was milled at 100 rpm for 30 min. The composite powders were compacted by extrusion at 623 K with respect to the formation of the crystalline $Al_7Cu_2Fe$ phase starting at temperatures higher than 673 K[53,54].

Figure 13a shows the cross section of an extruded $Al_{60}(Al_{0.63}Cu_{0.25}Fe_{0.12})_{40}$ rod. Although the particle dispersion in the aluminum matrix is relatively homogeneous, the size distribution (Fig. 13b) is rather heterogeneous. The majority of the particles has a size between 5 and 30 μm, but there are also particles with a size of around 50 μm or even more. A better homogenization would require extended milling, which is not helpful to yield a reasonable powder output. Moreover, the shape of the particles appears rather irregular, since the brittle quasicrystalline particles are shaped by particle cracking instead of plastic deformation as it would have been the case for a ductile component. No pores are observed in the matrix or along the particle-matrix interfaces, which points towards a density of the specimens of nearly 100 %. XRD analysis and SEM investigations on the powders before and after consolidation reveal no effect of the milling or the heat treatment during hot extrusion on the phase composition of the material.

Figure 14 shows plots of the true stress vs. the true compression of composites with 40, 50, 60 and 80 vol.% quasicrystalline phase. Despite differences in strength and compression strain, all the specimens exhibit a similar deformation behavior. After exceeding the yield point work hardening occurs, which decreases with increasing deformation until fracture of the material sets in. With this, the material does not show a pronounced ultimate strength which, therefore, equals to the maximum stress value before the material failure causes the stress reduction. The same observation has been reported for cast AlCuFe composites[42]. A remarkable high yield strength and ultimate strength of 567 MPa and 660 MPa, respectively, is reached for the $Al_{20}(Al_{0.63}Cu_{0.25}Fe_{0.12})_{80}$ sample. However, this goes along with a poor ductility of the composite of only 1.8%. The highest ductility of 25% is found for the $Al_{60}(Al_{0.63}Cu_{0.25}Fe_{0.12})_{40}$ sample, which on the other hand exhibits the lowest strength. The Youngs moduli of all samples are almost identical and with around 70 GPa equal to that of aluminum[33]. From the stress-compression curves it can be concluded that the deformation process is restricted to the aluminum matrix and can be considered as a flow of aluminum around the quasicrystalline particles. The correlation of the yield strength $\sigma_y$ and the ultimate strength $\sigma_{UCS}$ with the quasicrystalline volume fraction obeys a linear dependence according to a rule-of-mixtures.

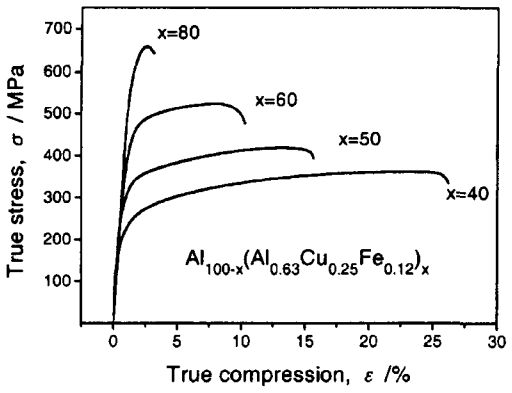


**Fig. 14. True stress vs. true compression plots obtained from room temperature constant rate compression tests of extruded AlCuFe composites with different Al-content.**

### 3.3. Enhanced Plasticity in a Ti-base Bulk Metallic Glass-forming Alloy by *in situ* Formation of a Composite Microstructure

Figure 15a shows the composite microstructures on sections of the as-cast 3 mm-diameter cylinders for the Ti-base BMG-forming alloy. The microstructure consists of a dendritic phase (dark) and a small amount of bright phase dispersed in the matrix (gray). The amount of dendritic phase is estimated to be about 80~90 vol.%, and the dendritic branches to be about 1-5 μm in size. Figure 15b shows a bright-field TEM image of this microstructure. The matrix includes glassy and crystalline phases. Figure 15c shows the selected-area diffraction pattern taken from the glassy phase. The glassy volume fraction in the alloy is determined by DSC analysis. The DSC traces reveal that the glass-to-crystalline transformation occurs around 758~778 K (heating rate 20 K/min). By comparing the enthalpy of the first exothermic peak of the as-cast cylinders with that of the melt-spun ribbon, the glassy volume fraction in the as-cast cylinders can be estimated to be about 11 vol.% for the 2 mm-diameter and only 6 vol.% for the 3 mm-diameter rods, respectively. Figure 15d shows

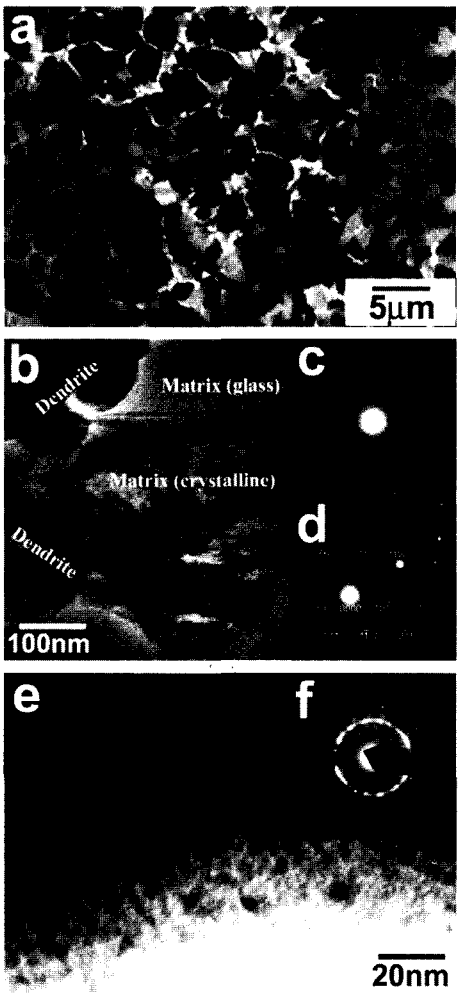


**Fig. 15. SEM backscattered electron image of the as-cast microstructure taken from the cross-section of a $Ti_{50}Cu_{23}Ni_{20}Sn_7$ 3 mm-diameter cylinder (a), the bright-field TEM image of the same microstructure (b), the selected-area diffraction pattern taken from the glassy phase in the matrix (c), the selected-area diffraction pattern taken along the [0001] zone axis of one of the dendrites corroborating the formation of a *hcp* phase (d), the bright-field TEM image of the nanocrystals in the matrix (e) and the selected-area diffraction pattern taken from the nanostructure (f).**

a selected-area diffraction pattern taken from a dendrite along the [0001] zone axis, which corroborates the *hcp* structure of the dendritic phase. The details of the crystalline phases in the matrix are observed by TEM, revealing a nanostructure with grain sizes of about 2-5 nm, as shown in Fig. 15e. Figure 15f shows the

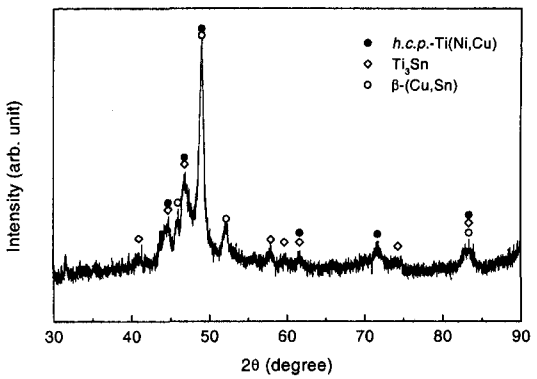


**Fig. 16. XRD pattern (Cu-Kα) of an $Ti_{50}Cu_{23}Ni_{20}Sn_7$ as-cast 3 mm-diameter cylinder.**

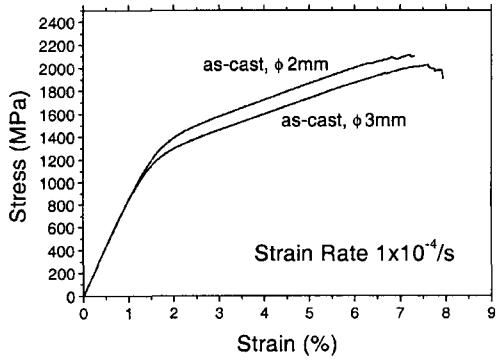


**Fig. 17. Room temperature compressive stress-strain curves for as-cast $Ti_{50}Cu_{23}Ni_{20}Sn_7$ cylinders.**

selected-area diffraction pattern taken from the nanostructure. XRD analysis indicates reflections of supersaturated *hcp* Ti(Ni,Cu) solid solution, $Ti_3Sn$ compound and β-(Cu,Sn) solid solution (Fig. 16). SEM electron microprobe analysis reveals the average composition of the dendritic phase to be $Ti_{51}Cu_{18.2}Ni_{28}Sn_{2.8}$ and of the white-colored phase to be $Ti_{54.6}Cu_{19}Ni_{6.4}Sn_{20}$, *i.e.* its Sn content is more than about three times the average alloy composition.

A series of compression tests at room temperature was carried out for this alloy. The as-cast 2 and 3 mm-diameter cylinders present significant work hardening and plasticity of about 6% plastic strain. Figure 17 shows the stress-strain curves for the 2 and 3 mm-diameter cylinders, respectively. The ultimate compression stress is as high as 2.03 GPa, which is significantly higher than the typical strength level of about 1.2 GPa for crystalline Ti alloys[6]. Yielding occurs at

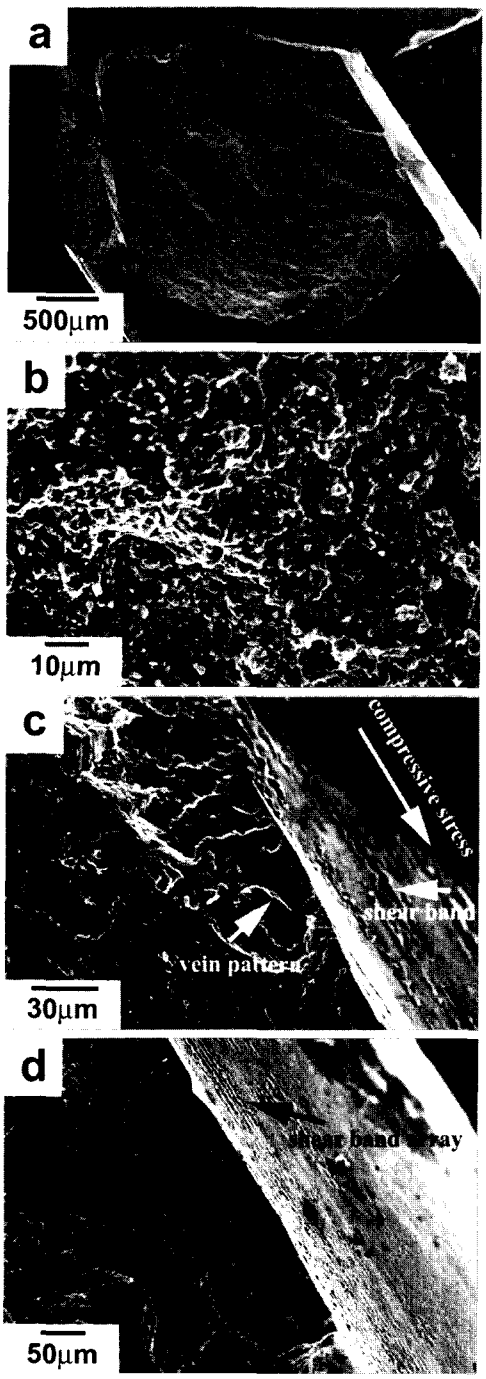


**Fig. 18. SEM images of the fracture surface of the as-cast 3 mm diameter $Ti_{50}Cu_{23}Ni_{20}Sn_7$ cylinder after compressive testing: (a) macro-appearance of the fracture surface, (b) typical fracture surface, (c) origination of the vein pattern and detail of the shear band, (d) shear band pattern array parallel to the compressive stress direction.**

about 1.19 GPa. The Youngs Modulus is 85.8 GPa, *i.e.* lower than that of fully glassy Ti-base BMGs (about 100 GPa)[6] but comparable to that of Zr-base BMGs, which is obviously lower than that of crystalline Ti-alloys (~120 GPa)[6]. The fracture occurs roughly along the plane of maximum stress as shown in Fig. 18a. The fracture surface displays typical skeleton-like soft networks (Fig. 18b) and vein patterns (Figs. 18c). The vein pattern originates from the shearing-off and ripping apart of the shear bands. This behavior is frequently observed for Zr-base BMGs[59]. However, a different feature is that the shear bands for the present partially glassy composite already experience too much deformation before ripping apart according to the evidence of the formation of protuberances in the shear bands spreading all over the surface of the samples, as shown in Figs. 18c and d. For single-phase BMGs, the deformation concentrates on one or several shear bands[11]. More deformation promotes more "work-softening" in the shear band(s), and finally leads to catastrophic fracture without obvious plastic strain. The other shear bands do not experience too much deformation, and no protuberance has been observed. For the present Ti-base composite, however, the existence of the dispersed dendritic crystallites phase can prevent the catastrophic failure by both obstructing the shearing-off of the shear bands and allows for significant work-hardening, resulting in a homogenous deformation over all the shear bands. Because of this, a well-developed shear band array with obvious protuberance is present on all the surfaces of the fractured samples.

## 4. Conclusions

$Mg_{55}Y_{15}Cu_{30}$ metallic glass matrix composites containing up to 30 vol.% $Y_2O_3$ particles were produced by MA. The presence of nanosized $Y_2O_3$ particles (about 10 nm), homogenously dispersed in the glassy matrix does not change the glass transition and the crystallization behavior significantly, although there may be some small amount of particle dissolution, which slightly changes the composition of the glassy matrix. The viscosity of the composites in the supercooled liquid state slightly increases with increasing volume fraction of $Y_2O_3$ particles. Nevertheless, bulk samples can be easily prepared by hot pressing. The $Y_2O_3$ additions increase the Vickers hardness and enhance the compression strength of the material compared to the dispersoid-free glass. The samples reach

very high strength values with a maximum of 709 MPa for the $Mg_{55}Y_{15}Cu_{30}$-5 vol.% $Y_2O_3$ composite. The room temperature strength is 1.5-2.5 times higher than the strength of conventional Mg-based cast alloys. The additions of $Y_2O_3$ dispersoids leads to distinctly higher compression strength compared to the particle-free alloy at higher temperatures slightly below $T_g$.

Nanoscale composites consisting of quasicrystalline particles incorporated in an Al-solid solution matrix were synthesized by melt spinning of Al-Mn-Ce alloys. Bulk samples were prepared by hot extrusion of powders, which were synthesized by BM of these ribbons. Although the extrusion temperature (623 K) was estimated from DSC analysis as sufficiently low to avoid changes of the composite microstructure, the precipitates grow to micrometer size upon consolidation. With a maximum ultimate strength of 975 MPa for $Al_{91}Mn_7Ce_2$ and a combination of a strength of 851 MPa with a ductility of 23 % for $Al_{92}Mn_6Ce_2$, outstanding mechanical properties have been achieved for these alloys, which can easily compete with the performance of state-of-the-art ceramic-reinforced Al-matrix composites. Furthermore, the formation of an icosahedral single-phase directly by MA of an $Al_{63}Cu_{25}Fe_{12}$ powder mixture was reported. As a striking feature, it developed from a disordered cubic phase with bcc structure incorporating all the three elements. Bulk micrometer-scale composites were obtained by blending the quasicrystalline powders with pure aluminum and hot extrusion. The mechanical properties, i.e. strength and ductility, can be tailored by changing the amount of Al-powder addition. The maximum achieved strength of 660 MPa for the $Al_{20}(Al_{0.63}Cu_{0.25}Fe_{0.12})_{80}$ composite represents the possibility to improve the strength of a pure element many times over its intrinsic property by a discontinuous reinforcement with quasicrystalline particles.

Finally, the $Ti_{50}Cu_{23}Ni_{20}Sn_7$ BMG-forming alloy can form a dispersed composite microstructure upon centrifugal and injection casting. The composite microstructure includes ductile precipitates of a dendritic *hcp* Ti solid solution and minor amounts of $Ti_3Sn$, β-(Cu, Sn) as well as glassy phase. The plastic deformability of the composite is enhanced compared to monolithic BMGs by the dispersion of the dendritic crystallites by avoiding highly localized shear bands under loading. The fracture surface presents typical skeleton-like networks. The shear bands over the entire surface of the samples are highly developed, indicating that deformation occurs via all shear bands, resulting in nearly 6% compressive plastic strain before failure. These results reveal the possibility of obtaining new BMG-base composites with complex crystalline phases/phase mixtures and good room temperature ductility by optimization of alloy composition and casting conditions.

## Acknowledgements

The authors thank M. Frey, H. Grahl, M. Gründlich, A. Güth, H.-J. Klauβ, U. Kühn, C. Mickel, S. Müller-Litvanyi, and H. Schulze for technical assistance, and S. Deledda, W. Löser, S. Scudino and N. Schlorke-de Boer for stimulating discussions. G. He is very grateful for the financial support of the Alexander-von-Humboldt Foundation. This research was sponsored by the German Science Foundation (DFG Schwerpunktprogramm "Quasikristalle"; contract Ec 111/8) and by the EU within the framework of the RTN-Network on bulk metallic glasses (HPRN-CT-2000-00033).

## References

1. W. J. G. Bunk: *Advanced Aerospace Materials*, H. Buhl (Ed.), Springer, Berlin, Heidelberg (1992) 1.
2. C. Suryanarayana (Ed.): *Non-Equilibrium Processing of Materials*, Pergamon Press, Oxford, U.K. (1999).
3. C. Suryanarayana: Prog. Mater. Sci., **64** (2001) 1.
4. J. S. Benjamin: Metall. Trans., **1** (1970) 2943.
5. W. L. Johnson: MRS Bull., **24** (1999) 42.
6. A. Inoue: Acta Mater., **48** (2000) 277.
7. T. Zhang, A. Inoue and T. Masumoto: Mater. Trans. JIM, **32** (1991) 1005.
8. A. Peker and W. L. Johnson: Appl. Phys. Lett., **63** (1993) 2341.
9. M. Seidel, J. Eckert and L. Schultz: J. Appl. Phys., **77** (1995) 5446.
10. J. Eckert: Mater. Sci. Eng., **A226-228** (1997) 364.
11. C. T. Liu, L. Heatherly, D. S. Eaton, C. A. Carmichael, J. H. Schneibel, C. H. Chen, J. L. Wright, M. H. Yoo, J. A. Horton and A. Inoue: Metall. Mater. Trans., **29A** (1998) 1811.
12. H. Kato and A. Inoue: Mater. Trans. JIM, **38** (1997) 793.
13. H. Choi-Yim and W. L. Johnson: Appl. Phys. Lett., **71** (1997) 3808.
14. H. Chen, Y. He, G. J Shiflet and S. J. Poon: Nature, **367** (1994) 541.
15. H. Choi-Yim, R. Busch, U. Köster and W. L. Johnson: Acta Mater., **47** (1999) 2455.

16. J. Eckert, A. Kübler and L. Schultz: J. Appl. Phys., **85** (1999) 7112.
17. C. Fan and A. Inoue: Mater. Trans. JIM, **40** (1999) 42
18. R. B. Dandliker, R. D. Conner and W. L. Johnson: J. Mater. Res., **13** (1998) 2896.
19. C. P. Kim, R. Busch, A. Masuhr, H. Choi-Yim and W. L. Johnson: Appl. Phys. Lett., **79** (2001) 1456.
20. R. D. Conner, R. B. Dandliker and W. L. Johnson: Acta Mater., **46** (1998) 6089.
21. C. C. Hays, C. P. Kim and W. L. Johnson: Phys. Rev. Lett., **84** (2000) 2901.
22. F. Szuecs, C. P. Kim and W. L. Johnson: Acta Mater., **49** (2001) 1507.
23. U. Kühn, J. Eckert, N. Mattern and L. Schultz: Appl. Phys. Lett., **80** (2002) 2478.
24. A. Inoue: Mater. Trans. JIM, **36** (1995) 866.
25. C. Fan, R. T. Ott and T. C. Hufnagel: Appl. Phys. Lett., **81** (2002) 1020.
26. J. Eckert, M. Seidel, A. Kübler, U. Klement and L. Schultz: Scripta. Mater., **38** (1998) 595.
27. S. Deledda, J. Eckert and L. Schultz: Mater. Sci. Forum, **360-362** (2001) 85.
28. B. Weiß and J. Eckert: J. Metastable and Nanocrystalline Mater., **343-346** (2000) 129.
29. S. Takeuchi and T. Hashimoto: Jpn. J. Appl. Phys., **32** (1993) 2063.
30. M. Feuerbacher, B. Baufeld, R. Rosenfeld, M. Bartusch, G. Hanke, M. Beyss, M. Wollgarten, U. Messerschmidt and K. Urban: Phil. Mag. Lett., **71** (1995) 91.
31. L. Bresson and D. Gratias: J. Non-Cryst. Solids, **153** (1993) 468.
32. U. Köster, W. Liu, H. Liebertz and M. Michel: J. Non-Cryst. Solids, **153-154** (1993) 446.
33. I. J. Polmear: *Light Alloys*, E. Arnold Ltd., London (1981).
34. P. Sainfort and B. Dubost: J. de Physique Colloque, **C3-9** (1987) 407.
35. P. Liu, A. H. Stigenberg and J. O. Nilson: Acta Metall. Mater., **43** (1995) 2881.
36. A. Inoue, M. Watanabe, H. M. Kimura, F. Takahashi, A. Nagata and T. Masumoto: Mater. Trans. JIM, **33** (1992) 723.
37. M. Watanabe, A. Inoue, H. M. Kimura T. Aiba and T. Masumoto: Mater. Trans. JIM, **34** (1993) 162.
38. A. Inoue, H. Kimura and K. Kita: *New Horizons in Quasicrystals*, A. I. Goldman, D. J. Sordelet, P. A. Thiel, J. M. Dubois (Eds.), World Scientific, Singapore (1997) 256.
39. F. Schurack, J. Eckert and L. Schultz: J. Metastable and Nanocrystalline Mater., **2-6** (1999) 49.
40. A. P. Tsai, K. Aoki, A. Inoue and T. Masumoto: J. Mater. Res., **8** (1993) 5.
41. S. M. Lee, J. H. Jung, E. Fleury, W. T. Kim and D. H. Kim: Mater. Sci. Eng., **A294-296** (2000) 99.
42. E. Fleury, S. M. Lee, W. T. Kim and D. H. Kim: J. Mater. Sci., **36** (2001) 963.
43. A. P. Tsai, A. Inoue and T. Masumoto: Jpn. J. Appl. Phys., **26** (1987) 1994.
44. F. Schurack, J. Eckert and L. Schultz: Acta Mater., **49** (2001) 1351.
45. X. H. Lin and W. L. Johnson: J. Appl. Phys., **78** (1995) 6514.
46. T. Zhang and A. Inoue: Mater. Trans. JIM, **39** (1998) 1001.
47. J. Eckert, N. Schlorke-de Boer, B. Weiß and L. Schultz: Z. Metallkde., **90** (1999) 908.
48. S. Deledda, J. Eckert and L. Schultz: Scripta Mater., **46** (2002) 31.
49. J. Eckert, A. Reger-Leonhard, B. Weiß and M. Heilmaier: Mater. Sci. Eng., **A301** (2001) 1.
50. R. Busch, W. Liu and W. L. Johnson: J. Appl. Phys., **83** (1998) 4134.
51. P. de Hey, J. Sietsma and A. van den Beukel: Acta Mater., **46** (1998) 5873.
52. F. Spaepen: Acta Metall., **25** (1977) 407.
53. R. Nicula, A. Jianu, G. Holzhüter, T. Barfels and E. Burkel: J. Metastable and Nanocrystalline Mater., **8** (2000) 27.
54. F. Faudot, A. Quivy, Y. Calvayrac, D. Gratias and M. Harmelin: Mater. Sci. Eng., **A133** (1991) 383.
55. D. Gratias, Y. Calvayrac, Q. Devaud-Rzepski, F. Faudot, M. Harmelin, A. Quivy and P. Bancel: J. Non-Cryst. Solids, **153-154** (1993) 482.
56. T. Ishimasa, Y. Fukano and M. Tsuchimori: Phil. Mag. Lett., **58** (1988) 157.
57. A. I. Salimon, A. M. Korsunsky, E. V. Shelekov, T. A. Sviridova, S. D. Kaloshkin, V. S. Tcherdyntsev and Y. V. Baldokhin: Acta Mater., **49** (2001) 1821.
58. N. Asahi, T. Maki, T. Matsumoto and S. Sawai: Mater. Sci. Eng., **A181/A182** (1994) 841.
59. Z. Bian, G. He and G. L. Chen: Scripta Mater., **46** (2002) 407.